Cavity quantum electrodynamics with quantum dots in microcavities

Gudat, J.

Chapter 3

Optical Modes in Oxide-Apertured Micropillars

This chapter is based on the submitted paper *Optical modes in oxide-apertured micropillars* (J. Gudat, C. Bonato, K. de Vries, D. Ding, H. Kim, S. M. Thon, P. M. Petroff, M. P. van Exter, D. Bouwmeester).

The central system for the research presented in this thesis is the oxide-apertured micropillar cavity with embedded self-assembled quantum dots, as illustrated in Fig. 3.1. The quantum dots confine the spin of either an electron or hole which is the *elementary qubit* of the system. In this architecture the single qubit and two-qubit operations are designed through optical interactions via micropillar cavity modes coupled to external modes. In order to make this process possible and scalable we need to understand and control both the quantum dot confined spin dynamics and the optical properties of the micropillar cavities in great detail. In Chap. 6 we give an overview of the rather complex dynamics of spins in quantum dots, and in this chapter we analyze the optical properties of micropillar cavities and their coupling to external modes. We show, using Gaussian beam calculations, that we can efficiently couple to the fundamental mode of a cavity which exhibits almost perfect Gaussian optical modes. Despite being mostly interested in the fundamental mode, a propagation model, which assumes cylindrical quadratic refractive index variation from the center of the cavity and yields Hermite-Gaussian solutions, is developed to explain the frequencies of the transverse modes. We show how well the experiments match the model for the lower order modes and present corrections to this model that allow to match higher order modes with better accuracy.

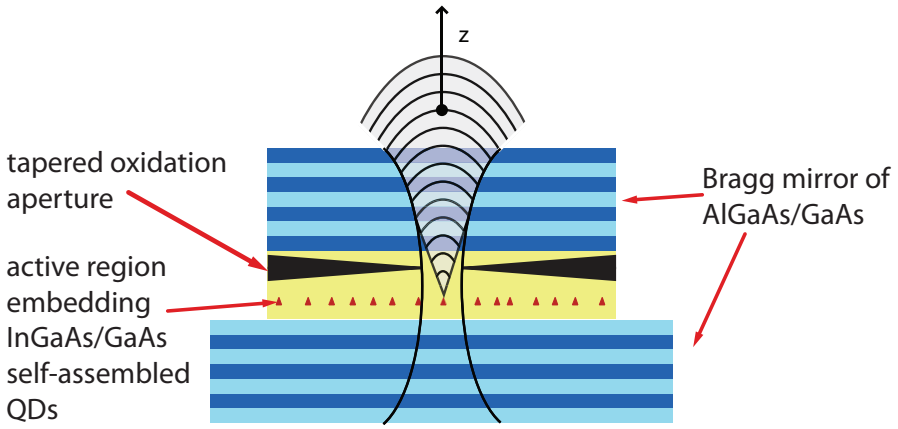

Figure 3.1: *Micropillar cavity scheme. The active layer carrying the quantum dots is sandwiched between top and bottom DBR mirrors. The wedged oxidation layer reaches almost to the center of the cavity and provides confinement of light in the z-direction. The QDs are located in the middle of the active layer below the oxidation layer.*

3.1 Introduction

The role of the micropillar cavities in our quantum information schemes is to enhance the optical interaction between a single embedded QD and an external optical mode. The cavity concentrates the light in the region of the quantum dot and if the coupling of light to the dipole moment of the quantum dot is strong enough it will influence the spontaneous emission properties of the quantum dot through the Purcell spontaneous emission enhancement factor P. As explained in Sect. 1.4, in order to implement efficient single-photon sources [56] and dipole-induced reflection [26] staying below the strong coupling regime it is desirable to have a significant Purcell factor. Since the Purcell factor is described by [53]

$$F_P = \frac{3}{4\pi^2}\left(\frac{\lambda}{n}\right)^3 \frac{Q}{V} \tag{3.1}$$

the cavity optical mode volume V needs to be reduced as much as possible, while keeping a high quality factor Q.

There are several types of cavities with the possibility to implement QDs as active emitters, for example photonic crystal membrane cavities [40,41], microtoroidal cavities [57] and micropillars [5]. Although micropillar cavities do not allow for the smallest possible mode volume, because the cavity optical field

extends into the Bragg mirror structure (leading to effective mode volumes typically of 4 to 8 cubic wavelengths instead of approximate 1 for photonic crystal membrane cavities), and their Q factors are currently limited to 150.000 [42] (significantly lower than the close to 1,000.000 Q-factors for certain Silicon based photonic membrane cavities and toroidal cavities), they do allow for integration of QDs and electrical gates that can control the electron charging of the QD and have the ability to mode match to external optical modes. These features outweigh the limitations in Q and V when considering implementation of scalable hybrid quantum information protocols [55] as described in Chap. 7.

Optical mode patterns in microcavities have been of interest for a long time in particular in oxide confined VCSEL structures [58–62]. We will describe the optical properties of the micropillar structure by the spectral and spatial properties of the electromagnetic modes. The typical modes for optical resonators with confocal mirrors and modeled in the paraxial beam approximation are the (Hermite) Gaussian modes. Such modes are mathematically very convenient to use. We will start our analysis by assuming that the oxidation taper will to first order be represented by a quadratically decreasing (radially from the center) refractive index, resulting in a Gaussian beam decomposition. We do not expect to have cylindrical symmetry around the optical axis due to the tensorial nature of the effective refractive index as a result of strain, crystal axis and asymmetry in the oxidation front. To first order we will simplify those complex effects by introducing an elliptical refractive index with the high and low refractive index along two orthogonal axis in the plane of the oxidation taper (perpendicular to optical axis). By comparing this first-order model with experimental data we obtain remarkable good agreement.

3.2 Oxide-apertured micropillars design and fabrication

Our micropillars are grown by molecular beam epitaxy on a GaAs [100] substrate with a 0.1μm buffer layer. Two distributed Bragg reflector (DBR) mirrors consisting of alternating layers of GaAs and $Al_{0.9}Ga_{0.1}As$ with a one-quarter optical thickness (32 pairs for the bottom DBR and 23 pairs for the top DBR), embed the aperture layer and the active layer with embedded InGaAs/GaAs self-assembled QDs. The DBR structure provides confinement of the light in the direction perpendicular to the active layer (the z-direction). Figure 3.2 presents details on the different layers. The alternating layers of $Al_{0.9}Ga_{0.1}As$ and GaAs have a thickness of 79.8 and 68.4nm. In the growth

direction, from bottom to top, the lower DBR stack is followed by a $\lambda/4$-thick $Al_{0.9}Ga_{0.1}As$ layer. The active region with one optical wavelength thickness embeds the self-assembled InGaAs/GaAs QDs (30Åthickness) in its center. The GaAs layer below and above the QDs are 135.4nm in thickness. The oxide aperture layer consists of graded-to-pure AlAs (100Å) sandwiched by a $Al_{0.75}Ga_{0.25}As$ below and a $Al_{0.8}Ga_{0.2}As$ followed by a $Al_{0.75}Ga_{0.25}As$ layer on top, resulting in a total thickness of three quarters optical wavelength. The aperture layer interfaces with a GaAs layer before the top DBR stack. This ensures that the thickness of the inner cavity length is multiples of $\lambda/2$ such that the mode distribution has anti-nodes at the first GaAs interfaces of the DBR stacks and is subject to a phase shift, which is the requirement for a cavity. Figure 3.3 illustrates the mode distribution of the cavity.

The QDs in the center of the active region are positioned to be at the maximum of the optical mode in the z-direction. This ensures optimal coupling efficiency between the QD excitons and the optical field. On the other hand the oxidation taper is located at a field node to reduce scattering and absorption losses due to the aperture. The cavity between the DBR mirrors causes a maximum in the optical density of states at the Bragg frequency (see the theoretical reflectivity spectrum in Fig. 3.4(a)). Multiple reflections from the repeating Bragg layers produce a standing wave for the normal incidence at the Bragg frequency, the resonance, and cause an electric field profile in the cavity as plotted in Fig. 3.4(b).

Different from conventional micropillar cavity structures [63] our cavities have trenches (Fig. 3.5 and Fig. 3.6) which are etched through the top DBR onto the bottom DBR and therewith define an oxidation front. Placed in an oxidation furnace, wet lateral oxidation converts the AlAs into Al_xO_y and therewith defines an oxidation front starting from the trenches leaving a small un-oxidized area in the center (see Fig. 3.7(b) for an SEM cross section image of a typical micropillar with fewer DBR mirrors). The oxidation is a rather slow process (depending on the parameter settings this process usually takes between 20 to 50 minutes) and can be calibrated to stop before it reaches the center of the cavity. Figure 3.7(a) schematically shows the oxidation layer in detail. An active area with an approximately circular central region of about 2 to 3μm in diameter (described by parameter d_{in}) stays untouched. The difference in effective refractive index is designed to be $\Delta n_{eff} = 0.08$ between the fully oxidized and the un-oxidized region. This provides an optical confinement effect in the x, y-plane [43, 44]. L_{taper} is the taper length of the oxide aperture (see Fig. 3.7(a)) and depends on the thickness and composition of the surrounding AlGaAs. It is designed to be approximately 1.5μm long after a 10μm oxidation. The effective mode Volume V_{eff} of the cavity directly

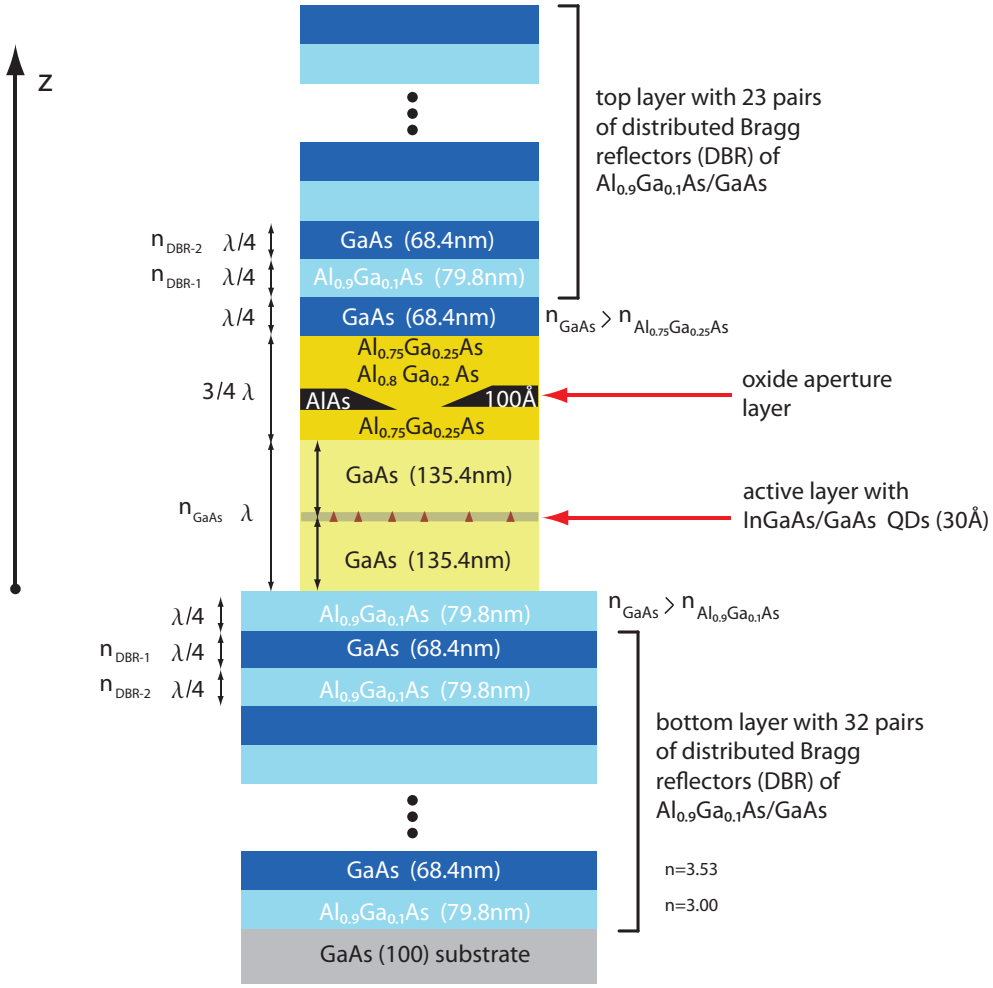

Figure 3.2: *Micropillar cavity layer details. The micropillar cavity consists of an active region with the embedded QDs at its center and an oxide aperture layer that are both sandwiched between distributed Bragg reflector mirrors. The active region is designed to be one λ optical wavelength thickness consisting of a 3nm thick QD layer centered between 135.4nm GaAs layers. On top of the active area is the oxide aperture. It is a thin 100Å thick AlAs layer that is surrounded by different compositions of AlGaAs. The designed optical thickness is $3/4\lambda$. The oxide aperture interfaces with a $\lambda/4$-thick GaAs layer.*

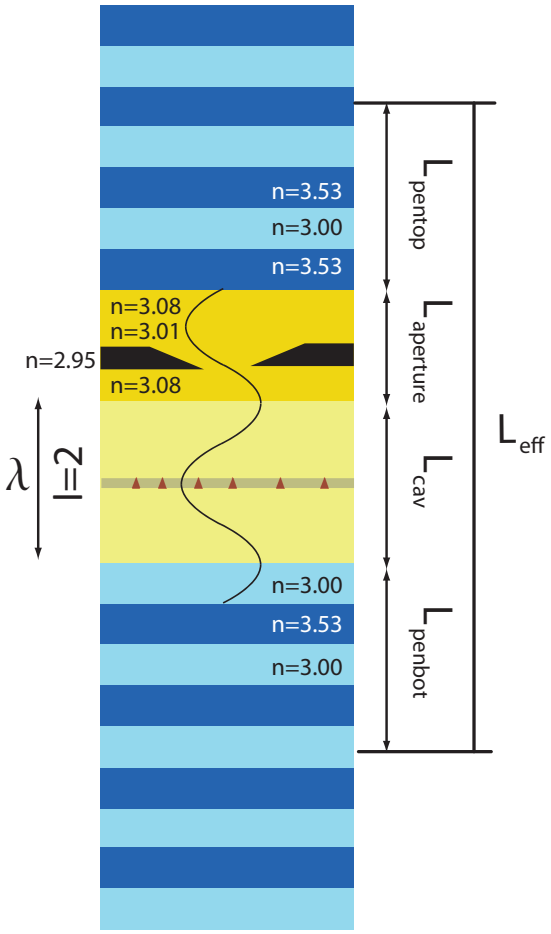

Figure 3.3: *Mode distribution and effective cavity length in the micropillar cavity. GaAs has a higher refractive index than* $Al_{0.9}Ga_{0.1}As$ *and* $Al_{0.75}Ga_{0.25}As$*. Therefore the lambda sized active region has a field maximum in the center where the QDs are positioned. Field maxima occur at the two interfaces with first* $Al_{0.9}Ga_{0.1}As$ *layer of the Bragg mirrors corresponding to* $l = 2$*. (see Sec. 3.3). Illustrated are the parts that contribute to the effective cavity length* L_{eff}*.*

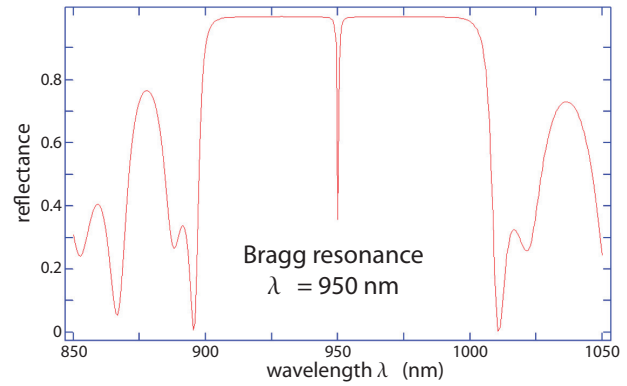

(a)

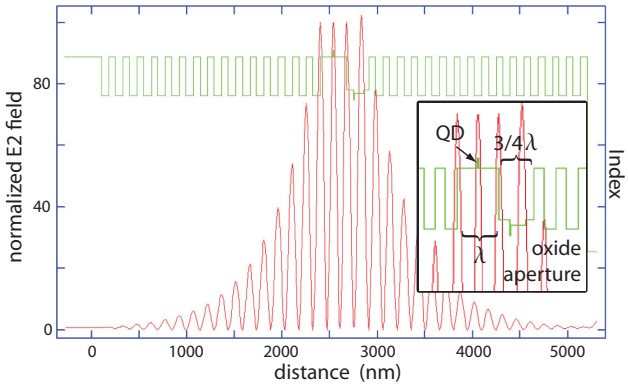

(b)

Figure 3.4: *Theoretical Bragg resonance and electric field profile conditions in the micropillars (courtesy of N.G. Stoltz). (a) Reflectivity spectrum for the oxide apertured microcavity with a resonance at the Bragg condition. (b) Normalized electric field profile in the microcavity for the Bragg wavelength at the normal incidence. The inset shows an enlargement of the cavity and aperture region. The λ-thick active region with the field maximum at the center at the position of the QDs is visible. The aperture is positioned at a node.*

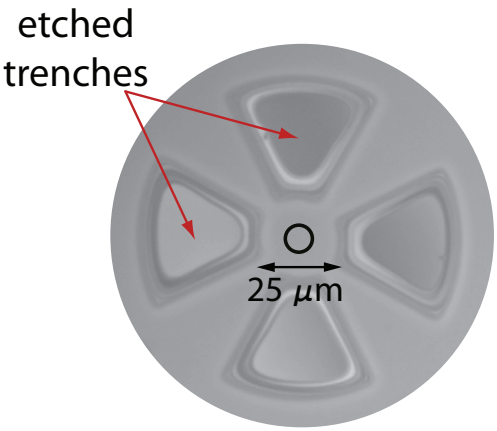

Figure 3.5: *Top view of a micropillar cavity image with four trenches. A circle in the center illustrates the position of the optical cavity.*

depends on the lateral mode radius. The quality factor Q is mostly determined by the optical scattering loss. Therefore control over the three parameters Δn_{eff}, d_{in} and $_{taper}$ is crucial for optimizing the cavity in order to enhance the Purcell factor that is proportional to $\frac{Q}{V_{eff}}$

One important parameter for further discussion in this chapter is the effective mode Volume V_{eff}. In order to calculate it, we need to know the effective cavity length L_{eff} in the z-direction. The parts that contribute to L_{eff} are illustrated in Fig 3.3. L_{penbot} and L_{pentop} are the penetration lengths of the modes in the bottom and the top DBR mirrors, L_{cav} and $L_{aperture}$ correspond to the height of the cavity and the aperture layer with the taper:

$$L_{eff} = L_{penbot} + L_{cav} + L_{aperture} + L_{pentop}. \tag{3.2}$$

L_{cav} and $L_{aperture}$ are known from the design. L_{penbot} and L_{pentop} are determined by

$$L_{pen} = \frac{\lambda}{4\Delta n} r_{dbr} \tag{3.3}$$

where r_{dbr} is the total mirror reflectivity. r_{dbr} is a function of the number of mirror periods (p) in a DBR mirror ($r_{dbr} = \frac{1-(n_1/n_2)^{2p}}{1+(n_1/n_2)^{2p}}$) and for our case is greater than 99%. Our cavities are designed to have a L_{eff} of 1.39μm.

To summarize, the oxide-aperture overcomes the limitations due to sidewall scattering loss typical in semiconductor etched micropillars [24] and avoids intrinsic scattering losses because of the designed null electric field value at the position of the oxide aperture (see Fig. 3.4(b)). At the same time, the aperture reduces the mode volume V in the lateral direction while maintaining high

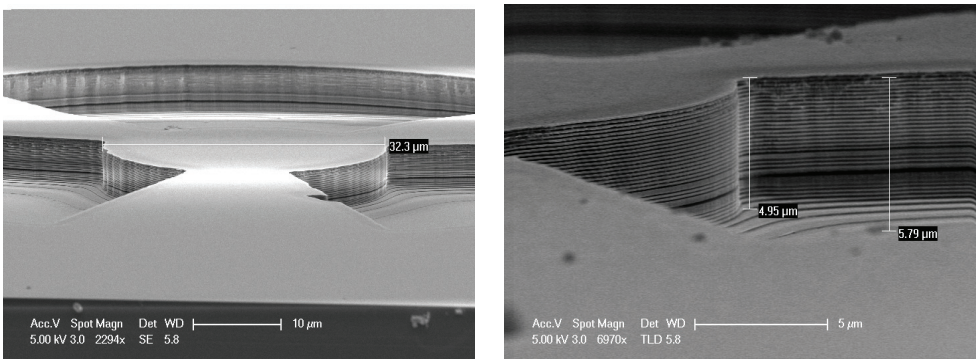

(a) (b)

Figure 3.6: *(a) SEM image of a cavity with three trenches from a bird's eye view. The diameter of the cavity center is* 32.3μm. *(b) SEM zoomed image of the cavity and one trench. The height of the trench is approximately* 5μm. *Courtesy of T.A. Truong, UC Santa Barbara.*

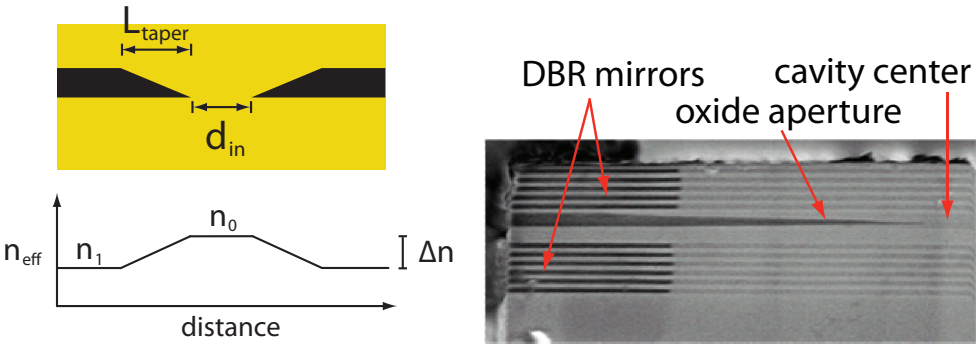

(a) (b)

Figure 3.7: *(a) Oxide aperture layer scheme with resulting effective refractive index profile. (b) SEM cross section image of a typical micropillar (with fewer DBR mirrors than used in the experiments). The oxide aperture in the middle has a linear profile in particular towards the center of the cavity where it stops before reaching the center and forms a very sharp edge. Courtesy of N.G. Stoltz.*

Q values. Additionally it is compatible with the implementation of electrical gates [56] for controlled electron charging of the QD and fine tuning of the frequency via the Stark effect. The cavity width after oxidation is approximately $2-4\mu$m compared to a smaller height of around 1μm. The oxide aperture is not perfectly circular, due to the anisotropic growth-rate of the oxide and the asymmetries in the shape and position of the trenches [64, 65]. Much effort is spent on optimizing the formation of the oxide-aperture [64, 65]. There have been various trials with different dimensions and shapes of the trenches to optimize the cavities properties including electrical gates [24, 56]. The samples investigated in this chapter partly had QDs embedded in their active region. However, for the understanding of the mode patterns analyzed in the following, the QDs were not addressed electrically.

3.3 Theoretical model of the optical modes

In order to describe the optical modes we first model the oxidation taper as an isotropic material with a quadratic refractive index profile (radially decreasing from the center) in the oxide aperture plane which we define as the x and y plane at the bottom center of the cavity. In the perpendicular z-direction the cavity with height h has a constant refractive index. The fundamental mode exhibits a Gaussian shape normal to the propagation direction, the z-direction. The approach is to solve the wave equation using an effective index model in the x, y-plane to describe the change of the refractive index $n(x, y)$ resulting from the oxidation taper [66, p. 640]

$$\nabla^2\mathbf{E}(\mathbf{r}) + k_0^2 n^2(x, y)\mathbf{E}(\mathbf{r}) = 0 \tag{3.4}$$

where the refractive index varies with the radial distance (r_x, r_y) from the center

$$n^2(x, y) = n_0^2\left(1 - \frac{x^2}{r_x^2} - \frac{y^2}{r_y^2}\right), \tag{3.5}$$

with n_0 the refractive index of GaAs. With other words, this expresses a constant refractive index in the z-direction and a quadratically decreasing index in the x, y-plane induced by the oxide aperture. Non-perfect symmetry is expressed by different radii r_x and r_y.
The vector wave equation becomes

$$\nabla^2\mathbf{E}(\mathbf{r}) + k^2\left(1 - \frac{x^2}{r_x^2} - \frac{y^2}{r_y^2}\right)\mathbf{E}(\mathbf{r}) = 0 \tag{3.6}$$

with $k = k_0 n_0$, where k_0 is the wave number in GaAs.

For the scalar part we assume solutions of the form

$$E(\mathbf{r}) = \psi_{[nm]}(x, y)\cos(\beta_l z) \tag{3.7}$$

where $z = 0$ is defined at one of the interfaces of the cavity region with the Bragg mirror. The factor

$$\beta_l = \frac{l\pi}{h} \tag{3.8}$$

indicates that $E(z)$ vanishes at the Bragg mirrors that are separated by an effective height h. The mode number of the z-component is indicated by $l = 1, 2, ...$ Since the QDs are grown in the middle of the cavity region we would like to have a field maximum at that position. Since the cavity region (GaAs) has a higher refractive index than AlGaAs of the first DBR layer there has to be field maxima at the interfaces. This makes a cavity of length λ the shortest cavity of interest for this project (see Fig. 3.3). This corresponds to $l = 2$.
If we write $\psi(x, y) = f(x)g(y)$ the wave equation (3.6) can be expressed as

$$\frac{1}{f}\frac{\partial^2 f}{\partial x^2} + \frac{1}{g}\frac{\partial^2 g}{\partial y^2} - \beta_l^2 + k^2\left(1 - \frac{x^2}{r_x^2} - \frac{y^2}{r_y^2}\right) = 0. \tag{3.9}$$

This equation can be split into a x- and a y-dependent part

$$\frac{1}{f}\frac{d^2 f}{dx^2} + k^2 - \beta_l^2 - \frac{k^2 x^2}{r_x^2} = C \tag{3.10}$$

$$\frac{1}{g}\frac{d^2 g}{dy^2} - \frac{k^2 y^2}{r_y^2} = -C \tag{3.11}$$

with C being a constant. We first consider Eq. (3.11). By introducing

$$\xi = \alpha_y y \quad \text{and} \quad \alpha_y \equiv \left(\frac{k}{r_y}\right)^{\frac{1}{2}}, \tag{3.12}$$

it follows for Eq. (3.11)

$$\frac{d^2 g}{d\xi^2} + \left(\frac{C}{\alpha_y^2} - \xi^2\right) g = 0. \tag{3.13}$$

This equation can be solved comparing it to the Schrödinger equation for a harmonic oscillator [66]. For C/α_y^2 we get

$$\frac{C}{\alpha_y^2} = 2m + 1, \tag{3.14}$$

where $m = 0, 1, 2, \ldots$. The corresponding eigenfunctions are

$$g_m(\xi) = H_m(\xi) e^{-\xi^2/2} \tag{3.15}$$

with $H_m(\xi)$ being the familiar Hermite polynomial of order m.
Defining

$$\zeta = \alpha_x y \quad \text{and} \quad \alpha_x \equiv \left(\frac{k}{r_x}\right)^{1/2} \tag{3.16}$$

Eq. (3.10) becomes

$$\frac{d^2 f}{d\zeta^2} + \left(\frac{k^2 - \beta_l^2 - C}{\alpha_s^2} - \xi^2\right) f = 0 \tag{3.17}$$

which gives

$$\frac{k^2 - \beta_l^2 - C}{\alpha_x^2} = 2n + 1 \tag{3.18}$$

with the corresponding eigenfunctions

$$f_n(\zeta) = H_n(\zeta) e^{-\zeta^2/2} \tag{3.19}$$

Eventually with Eqs. (3.19) and (3.15) for $\psi(x, y)$ we get a solution for the original wave function. The solution describes the component of the wave function transversal to the propagation direction z

$$\psi_{[nm]}(x, y) = H_n\left(\frac{\sqrt{2}x}{w_x}\right) H_m\left(\frac{\sqrt{2}y}{w_y}\right) e^{-\left(\frac{x^2}{w_x^2} + \frac{y^2}{w_y^2}\right)}, \tag{3.20}$$

where H_n and H_m are the *Hermite-Gaussian* functions of order n and m. $w_{x,y}$ is a measure for the *spot size* of a mode and can be calculated by

$$w_{x,y} = \frac{\sqrt{2}}{\alpha_{x,y}} = \sqrt{\frac{2r_{x,y}}{k}} \tag{3.21}$$

with k being the wave number.
Figure 3.8 shows the solutions for the wave equation (3.6) assuming a spot size of the mode with $w_x = w_y = 1/\sqrt{2}$.

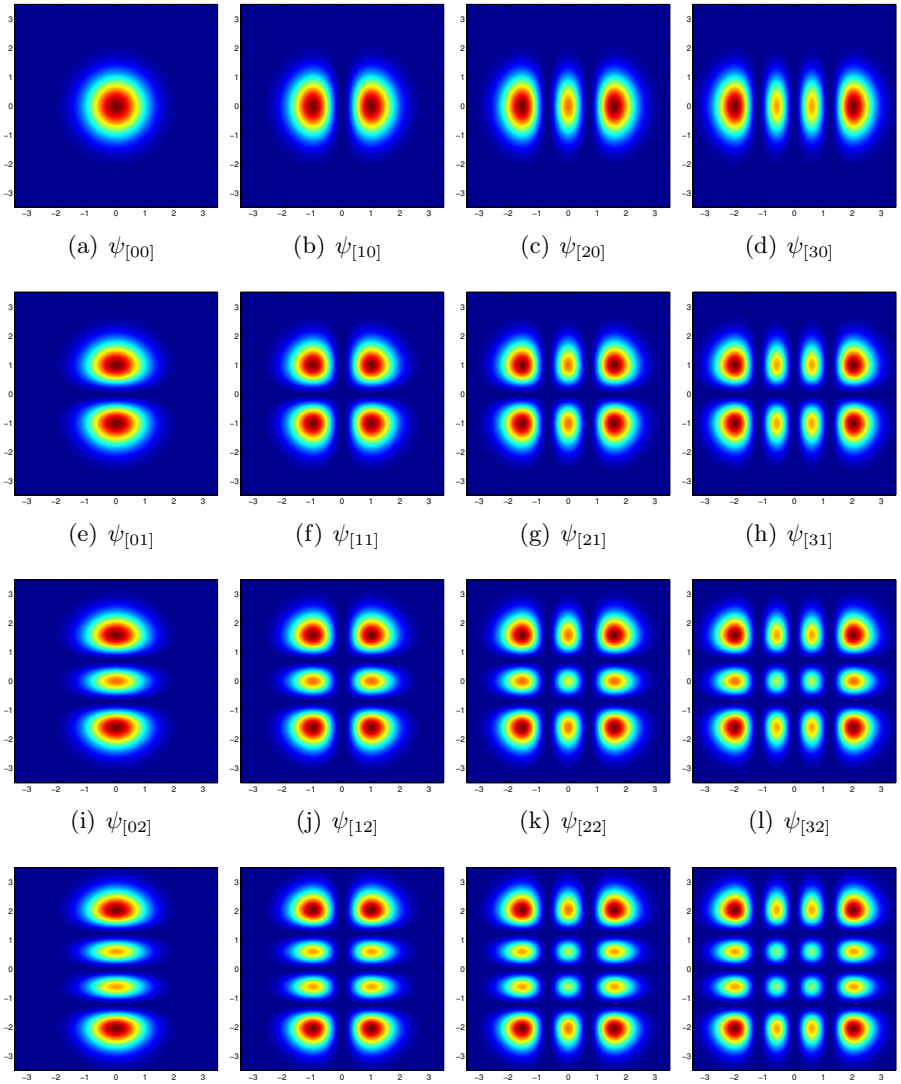

(a) $\psi_{[00]}$ (b) $\psi_{[10]}$ (c) $\psi_{[20]}$ (d) $\psi_{[30]}$

(e) $\psi_{[01]}$ (f) $\psi_{[11]}$ (g) $\psi_{[21]}$ (h) $\psi_{[31]}$

(i) $\psi_{[02]}$ (j) $\psi_{[12]}$ (k) $\psi_{[22]}$ (l) $\psi_{[32]}$

(m) $\psi_{[03]}$ (n) $\psi_{[13]}$ (o) $\psi_{[23]}$ (p) $\psi_{[33]}$

Figure 3.8: *Examples of Hermite-Gaussian solutions for the wave equation* (3.6)*:* $\psi_{[nm]}(x,y) = H_n\left(\frac{\sqrt{2}x}{w_x}\right) H_m\left(\frac{\sqrt{2}y}{w_y}\right) e^{-\left(\frac{x^2}{w_x^2}+\frac{y^2}{w_y^2}\right)}$*. The spot size of the mode given by Eq.* (3.21) *is set to* $w_x = w_y = 1/\sqrt{2}$*. The x- and the y-axis indicate the values for* x *and* y*.*

3.3.1 Theoretical spectrum of the modes

The mode spectrum of the cavity can be derived from the eigenvalues of the eigenfunctions. In order to do so we need to solve k respectively λ for a certain combination of n and m. From Eqs. (3.18) and (3.14) it follows

$$k^2 - \beta_l^2 - \alpha_y^2 (2m+1) = \alpha_x^2 (2n+1) \tag{3.22}$$

or

$$k^2 - 2\gamma k - \beta_l^2 = 0 \tag{3.23}$$

with $\gamma = \frac{1}{2} \cdot \left[\frac{(2n+1)}{r_x} + \frac{(2m+1)}{r_y} \right]$. Solutions for Eq. (3.23) are

$$k = \gamma \pm \sqrt{\gamma^2 + \beta_l^2}. \tag{3.24}$$

With $\lambda = \frac{2\pi}{k}$ and assuming weak index guiding the wavelength λ in GaAs for the mode number n, m, l can be expressed as

$$\lambda_{[nml]} = \frac{2\pi}{\frac{1}{2}\left[\frac{(2n+1)}{r_x} + \frac{(2m+1)}{r_y} \right] \pm \sqrt{\frac{1}{4} \cdot \left(\frac{(2n+1)}{r_x} + \frac{(2m+1)}{r_y} \right)^2 + \left(\frac{l\pi}{h} \right)^2}} \tag{3.25}$$

We can simplify this model knowing that the light is pre-dominantly confined to the lambda-sized GaAs central region in the z-direction. As explained above we use $l = 2$ in order to have a field maximum at the QD layer in the center of the GaAs (see Fig. 3.2).
Equation (3.25) can be further simplified assuming the width of the cavity to be reasonable larger ($\approx 5\mu$m) compared to the height of h of the cavity ($\approx 1\mu$m).
With $\gamma \sim \frac{1}{r_{x,y}}$ and $\beta_{l=2} \sim \frac{1}{h}$ we may expect that $\gamma < \beta$.
Given this assumptions and keeping in mind that $k > 0$, Eq. (3.24) becomes

$$k = \gamma + \beta_l \left(1 + \frac{1}{2}\frac{\gamma^2}{\beta_l^2} + ... \right) = \beta_l \left(1 + \frac{\lambda}{\beta_l} + \frac{1}{2}\frac{\gamma^2}{\beta_l^2} + ... \right) \tag{3.26}$$

resulting in

$$\lambda = \frac{2\pi}{k} = \frac{2\pi}{\beta_l} \left(\frac{1}{1 + \frac{\gamma}{\beta_l} + \frac{1}{2}\frac{\gamma^2}{\beta_l^2} + ...} \right) \approx \frac{2h}{l} \left(1 - \frac{\gamma}{\beta_l} \right). \tag{3.27}$$

Re-substituting γ and with the wavelength in GaAs being $\lambda_0 = n_0 \lambda$ the wavelengths of the various modes are given by:

$$\lambda_{[nml],0} = n_0 \left(\frac{2h}{l} - \frac{h^2}{\pi l^2} \left\{ \frac{(2n+1)}{r_x} + \frac{(2m+1)}{r_y} \right\} \right). \tag{3.28}$$

The label $[nml]$ indicates the mode numbers of the $x-, y-$, and $z-$component while the 0 indicates this being the wavelength in GaAs.
For a given mode in the z-direction the predicted wavelength for isotropic materials in vacuum becomes

$$\lambda_{[nml]} = \lambda_{[00]} - an - bm = \lambda_{[00]} - \frac{n_0 h^2}{2\pi l^2}\left(\frac{n}{r_x} + \frac{m}{r_y}\right) \tag{3.29}$$

with

$$a = \frac{2n_0 h^2}{\pi r_x l^2} \tag{3.30}$$

$$b = \frac{2n_0 h^2}{\pi r_y l^2} \tag{3.31}$$

$$\lambda_{[00]} = \frac{2n_0 h}{l} - \left(\frac{a+b}{2}\right). \tag{3.32}$$

3.3.2 Anisotropic materials

So far we considered an isotropic refractive index which is not dependent on the polarization of the light. Since we aim for polarization degenerate fundamental modes (see Chap. 1) we need to carefully analyze polarization effects. A description for anisotropic materials can be obtained modeling the geometry and strain by a position dependent dielectric tensor introducing polarization into the discussion. We replace $k_0^2 n^2(x,y)$ by the tensor

$$\epsilon = \begin{pmatrix} \epsilon_{xx} & 0 \\ 0 & \epsilon_{yy} \end{pmatrix} \tag{3.33}$$

with

$$\epsilon_{xx}(x,y) = \epsilon_m \left(1 - \frac{x^2}{r_{xX}^2} - \frac{y^2}{r_{yX}^2}\right) \tag{3.34}$$

$$\epsilon_{yy}(x,y) = \epsilon_m \left(1 - \frac{x^2}{r_{xY}^2} - \frac{y^2}{r_{yY}^2}\right) \tag{3.35}$$

where X and Y indicate orthogonal linear polarizations with their predicted wavelengths

$$\lambda_{[nm]X} = \lambda_{[00]X} - a_X n - b_X m \tag{3.36}$$

$$\lambda_{[nm]Y} = \lambda_{[00]Y} - a_Y n - b_Y m. \tag{3.37}$$

The orientation of the axes will be determined by geometry, strain, and oxidation. This is highly complicated and we therefore use experimental data to determine the orientation.

3.3.3 Relative mode splitting and Purcell factor

The factors a and b in Eq. (3.30) and (3.31) describe the relative mode splitting between the fundamental mode and the first order modes:

$$a = \Delta\lambda_x = \lambda_{[00]} - \lambda_{[10]} \tag{3.38}$$
$$b = \Delta\lambda_y = \lambda_{[00]} - \lambda_{[01]}. \tag{3.39}$$

According to Eq. (3.21) we know that the radii $r_{x,y}$ can be expressed as

$$r_{x,y} = \frac{\pi w_{x,y}^2}{\lambda}. \tag{3.40}$$

We get a direct link between the relative spacing of the transverse modes and the spot size w. It follows

$$\Delta\lambda_{x,y} = \frac{2n_0}{\pi r_{x,y}} \cdot \frac{h^2}{l^2} = \frac{\lambda_0^3}{2\pi^2 n_0 w_{x,y}^2} \tag{3.41}$$

with

$$\frac{h}{l} = \frac{\lambda_0}{2n_0}. \tag{3.42}$$

where λ_0 is the vacuum wavelength and n_0 the refractive index in GaAs. This assumes the boundary conditions for the optical mode $l = 2$ to be the height of the active cavity region with one optical wavelength thickness (following our discussion in the previous section). If we rewrite Eq. (3.41) as

$$\frac{\Delta\lambda_{x,y}}{\lambda_0} = \frac{1}{2n_0} \cdot \left(\frac{\lambda_0}{\pi w_{x,y}}\right)^2 \tag{3.43}$$

we can directly obtain the spot size of the mode by evaluating the relative splitting: a smaller splitting corresponds to a larger waist.

For determination of the Purcell factor we have to measure the quality factor Q and calculate the effective mode volume V_{eff} of the fundamental mode. For the latter we assume a cylindrical approximation. Therefore we have to combine the transverse mode area with the longitudinal size L_{eff} given by Eq. (3.2). As the time-averaged intensity distribution for Gaussian beams is $I(x,y) = I_0 e^{-\left(\frac{2x^2}{w_x^2}+\frac{2y^2}{w_y^2}\right)}$, the effective transverse mode area corresponds to $\frac{\pi}{2} w_x w_y$. Hence, the effective mode volume becomes

$$V_{eff} = \frac{\pi}{4} w_x w_y L_{eff} \tag{3.44}$$

where the additional factor 1/2 stems from the fact that the effective mode volume is composed of nodes and antinodes [67]. With Eq. (3.41) V_{eff} can be expressed as

$$V_{eff} = \frac{\lambda_0^3}{8n_0\pi} \cdot \frac{1}{\sqrt{\Delta\lambda_x \cdot \Delta\lambda_y}} \cdot L_{eff}. \tag{3.45}$$

Thus, the Purcell factor for coupling to an embedded emitter scales linearly with the transverse mode splitting $P \sim (\Delta\lambda/\lambda)$. This relation allows for a fast evaluation of our cavities during characterization of our samples. The larger the transverse mode splitting, the higher the Purcell factor.

3.4 Measurements

The optical modes are investigated by pumping the structure non-resonantly (785 nm, above the GaAs bandgap) with a few mW laser power and spectrally characterizing the photoluminescence with a spectrometer (resolution 0.016 nm/pixel) input coupled by a single-mode fiber. The pump beam is tightly focused on the sample by a high-NA aspheric lens (focal length $f_0 = 4.2$ mm, NA = 0.6) or an objective (focal length $f_0 = 3.5$ mm, NA = 0.8). In order to have a spatially-resolved photoluminescence plot, the excitation beam is scanned utilizing a piezo-driven xy-stage at a step size of 0.1μm over an area of $10 \times 10\mu$m. The spatial resolution is limited by the size of the excitation laser spot ($\approx 1\mu$m) on the sample. The repeatability of the positioning stage and its resolution is much better than our scanning steps (compare Sect. 2.2 in Chap. 2). Optimal focusing and a high stability over the time of the scanning procedure which takes up to a few hours when imaging large areas at high resolution is required for optimal results. For polarization resolved measurements, an analyzer, consisting of a fixed linear polarizer and a rotating half-wave plate, is placed in the collection path to account for the fact that a spectrometer is generally polarization dependent. Once a spectrum for each coordinate has been recorded we can compile density plots of specific optical modes by extracting the intensity of the specific wavelength from each spectrum and map these to the coordinate accordingly. Figure 3.9 shows a typical set of polarization resolved spectra of the same cavity. Figure 3.10 illustrates the typical mode order that we assume for a specific wavelength as modeled in the previous section according to Eq. (3.25). In this case r_x is larger than r_y resulting in a mode order of $00, 10, 01, ...$ from higher to smaller wavelength. When measuring the spectra optimization of the focus and the position of the sample is done in such a way that the count rate for the fundamental mode is maximized. As the whole spectrum is recorded at each position during a spatial scan, 2D images of the optical modes for any given wavelength can be

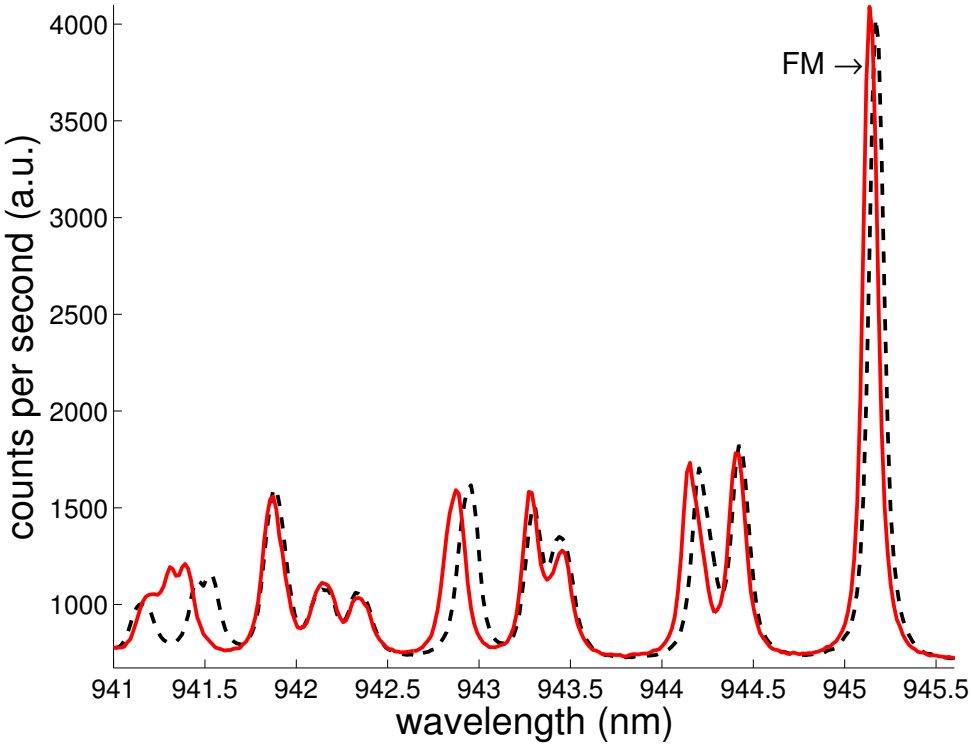

Figure 3.9: *Polarization resolved spectra for the two orthogonally polarized fundamental modes.*

extracted. Measurements have been carried out at room temperature and at 4K showing the same features though at low temperatures the spectra exhibit a much better signal to noise ratio and shift to lower wavelength. All results presented here were recorded at 4K.

3.5 Results

For a non-polarization resolved measurement with a scanning area of $10 \times 10 \mu$m with a step size of 0.1μm the results are presented in Fig. 3.11. Each spectrum is recorded with an integration time of $1s$. In addition to integrating the counts on the CCD array the scanning procedure typically adds a few more tens of a second for moving and settling the scanning stage. In total the scan took approximately 6 hours in which the experimental setup shows a high stability even at low temperatures. In other words, the scanning method measures the

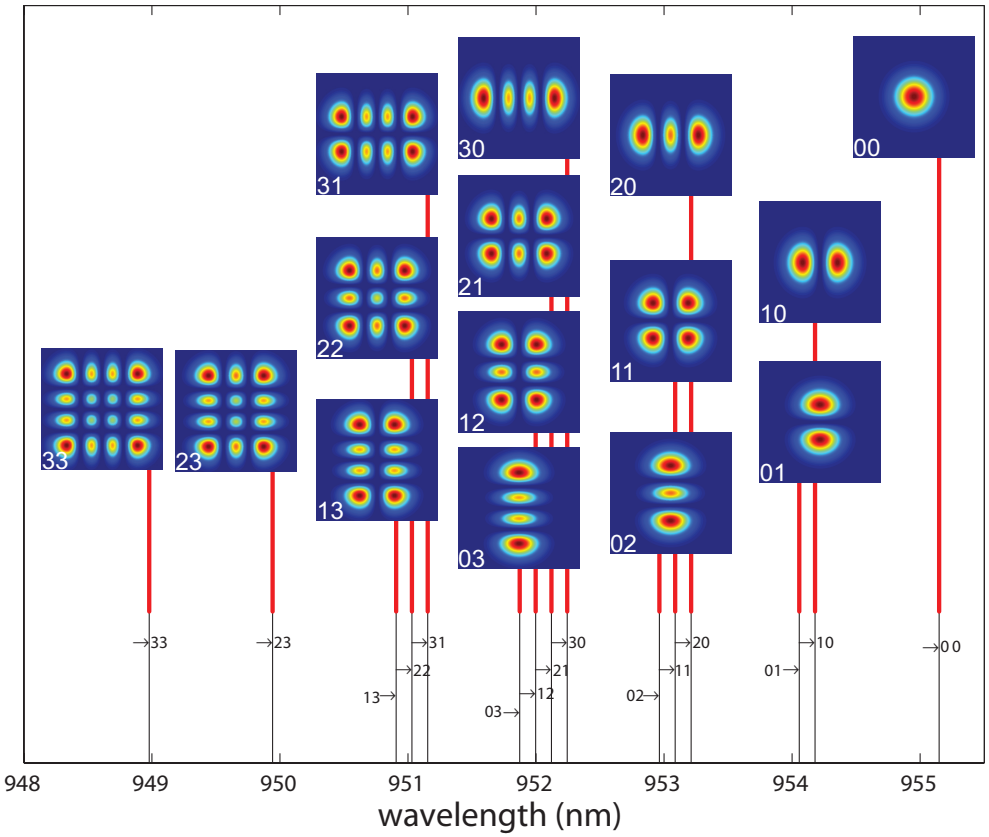

Figure 3.10: *Theoretical predictions of the mode order and their corresponding wavelength for $r_x > r_y$ according to Eq.* (3.25) *up to mode* 33.

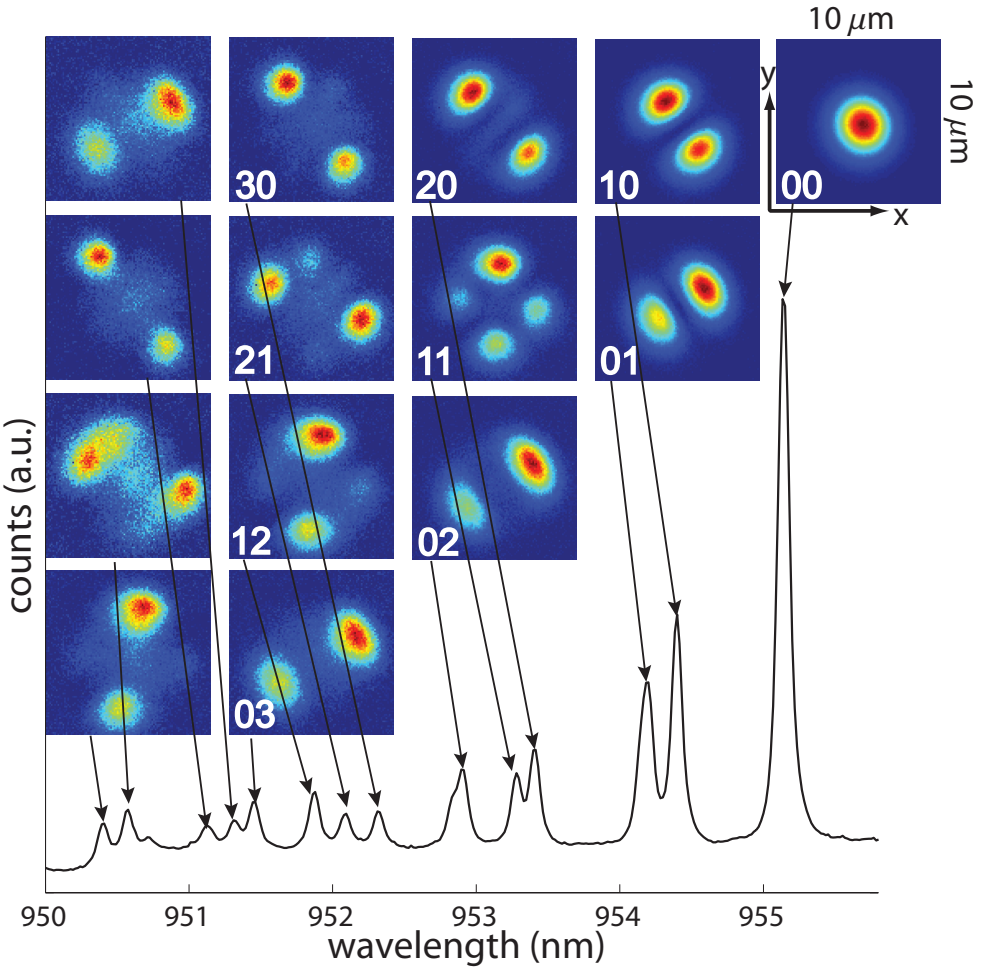

Figure 3.11: *Non-polarization resolved spatial scan of* $10 \times 10\mu m$ *with a step size of* $0.1\mu m$*. The optical mode for a given wavelength can be composed of the intensity measured at each position for that specific wavelength. The lower order modes (higher wavelength) can clearly be identified in accordance with the model established in this chapter and illustrated in Fig. 3.10. For higher order modes the resolution of the scans limit explicit identification.*

spectrum at each position causing a 6 hour time difference between the upper left and lower right density pixel. A high symmetry in the spatial images accounts for positional stability. Similar count rates at different positions for the same mode are an indication for the temperature stability over time. Comparing the upper part of the 2D spatial images with the lower part the latter ones exhibits a lower count rate. Temperature fluctuations of up to 2K were adjusted for and cause little change in the count rate. But the whole setup takes more than an hour to reach a temperature equilibrium. In the meantime the sample can get slightly out of focus without readjustment. Keeping the right focus over the whole time of the scan is difficult. Nevertheless, the 00 mode shows an equally symmetric high count rate everywhere.

Two-dimensional spatial images are shown for the peaks of the spectrum. The spatial scans of the first ten peaks show clear features of Hermite-Gaussian modes and allow mode identification when comparing with the projected modes in Fig. 3.10. With increasing mode order the scanning resolution limits definite identification. Given an unequal radius of r_x and r_y the mode order is exactly measured as projected by the model in the previous section. (Higher order modes as i.e. the 40, the 04 and so forth are expected to show up at smaller wavelengths than the modes illustrated.)

Investigating the potential of efficiently coupling external modes to the microcavity we fit a Gaussian to the spatial scan of the fundamental mode, the TEM 00 mode. Figure 3.12 shows the spatial scan for the 00 mode in higher resolution. (a) shows the $10 \times 10\mu$m scan with a step size of 0.1μm. The red lines cross the center of the peak at its maximum and illustrate the data points that are extracted to fit the 0-order Hermite-Gaussian (HG) function $H_0(x)e^{-\frac{x^2}{2}}$ as shown in figures (b) and (c). For the fundamental TEM 00 cavity mode the overlap accuracy of the Hermite-Gaussian model with the measurement is $99.94 \pm 0.06\%$ in the $x-$ and $99.93 \pm 0.06\%$ in the $y-$direction. This important result allows to make a clear statement for the efficiency of coupling an external fields to the cavity. Matching an external field to the cavity with a very high accuracy is decisive for the fidelity of the entanglement process described in Chap. 7. This is extremely important for applications because mode-matching is easy using Gaussian beams for coupling to external fields. The next higher order mode, the 10 mode, is fitted by a Hermite-Gaussian $H_1(x)e^{-\frac{x^2}{2}}$ with an overlap of $98.5 \pm 0.7\%$ (see Fig. 3.13).

From Gaussian fitting of the first three modes shown in measurement Fig. 3.11 and using Eq. (3.28) for those modes we determine the height of the cavity to be $h = 955.99 \pm 0.01$nm. Gaussian fitting of the intensity profile of

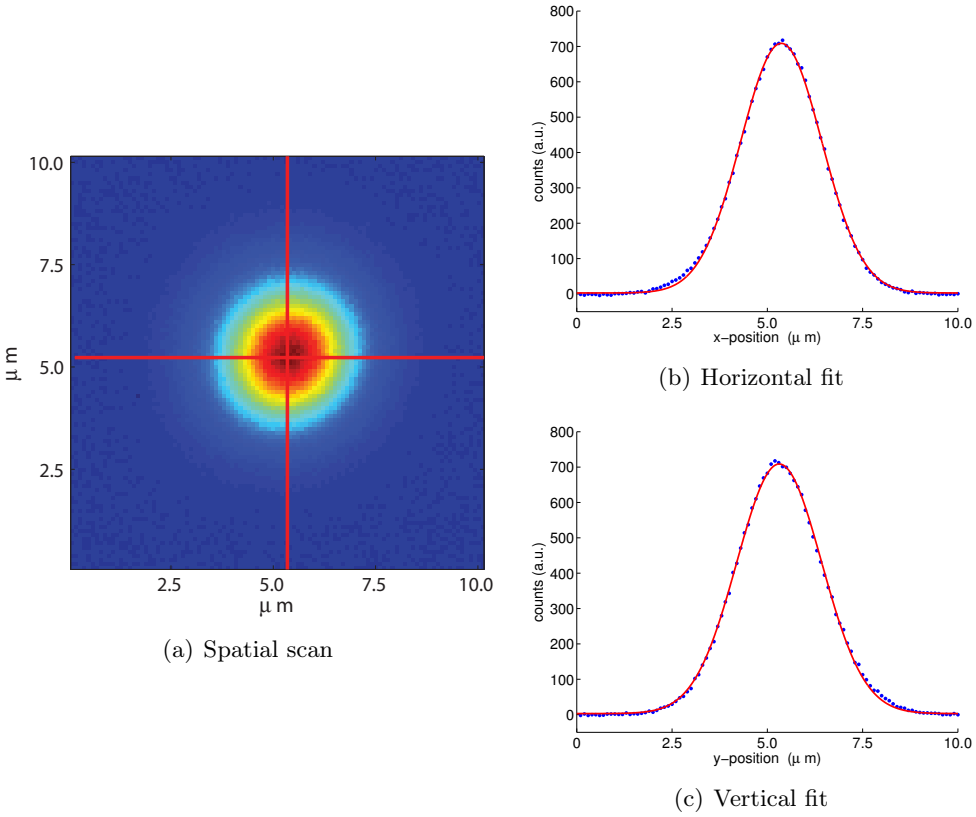

(a) Spatial scan

(b) Horizontal fit

(c) Vertical fit

Figure 3.12: *Spatial scan of HG00 mode with a Hermite-Gaussian fit according to* $H_0(x)e^{-\frac{x^2}{2}}$. *(a) Spatial scan area of* $10 \times 10\mu m$ *with a step size of* $0.1\mu m$. *The red lines illustrate the data points that are extracted to fit the Gaussian as shown in (b) and (c). The fits have an overlap accuracy of the Hermite-Gaussian mode of* $99.94 \pm 0.06\%$ *in* $x-$ *and* $99.93 \pm 0.06\%$ *in the* $y-$*direction, indicating a potentially high efficiency to couple external fields to the cavity.*

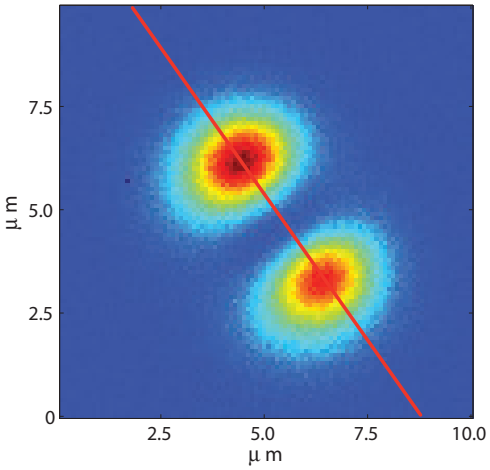

(a) Spatial scan

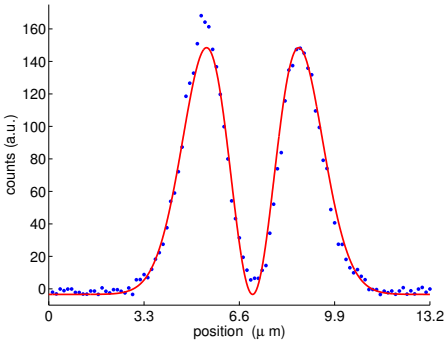

(b) Hermite-Gaussianfit

Figure 3.13: *Spatial scan of HG10 mode with Hermite-Gaussian fit according to* $H_1(x)e^{-\frac{x^2}{2}}$. *(a) Spatial scan area of* $10 \times 10\mu m$ *with a step size of* $0.1\mu m$. *The red line illustrates the data points extracted for the fit presented in (b). The fit has an overlap accuracy of the Hermite-Gaussian mode of* $98 \pm 0.07\%$.

the fundamental mode ($FWHM = \sqrt{2\ln 2} \cdot w_{x,y}$) shown in the measurement of Fig. 3.11 yields a spot size of $w_x \approx 2.13 \pm 0.08$ μm and $w_y \approx 2.25 \pm 0.09$ μm which compares to the calculated widths $w_x \approx 2.09$ μm and $w_y \approx 2.37$ μm extracted from the transverse mode splitting using Eq. (3.43). That is a deviation of less than 6% and emphasize the validity of the equation. Inserting Eq. (3.44) in Eq. (3.1) we can determine the maximum achievable Purcell factor

$$F_P = \frac{3}{4\pi^3}\left(\frac{\lambda_0}{n_0}\right)^3 \frac{4Q}{w_x \cdot w_y \cdot L_{eff}}. \tag{3.46}$$

We measure a Q of 11000 and with an effective cavity length of 1.39μm this measurement yields a Purcell factor of 4. This cavity, however, has a relatively small transverse mode splitting compared to other cavities investigated that showed mode splittings up to 4 times larger, resulting in Purcell factors as high as 16. Usually, the Purcell factor evaluation does not include discussion about any polarization dependance. But we have to keep in mind that in case of coupling to a circularly polarized transition (e.g. the QD trion state) and a linearly polarized non-degenerate cavity mode, the Purcell factor multiplies by an additional factor 1/2.

To this point, the results led to two conclusions. First, the spatial scans

confirm Hermite-Gaussian profiles. And second, the expected sequence of modes is correctly predicted. The following data investigates how well the wavelength for each mode is projected by the model. Figure 3.14 shows a polarization resolved spectrum with a longer wavelength range as compared to the previous graphs. All modes potentially covering the wavelength range shown are projected by the model and illustrated by vertical lines at their expected wavelength. The first three modes (from higher to lower wavelength) are identified as the 00, the 01 and the 10 mode and serve for extracting the three parameters r_x, r_y and h that are used to compute all higher order modes. Given this procedure for the first three modes the wavelength fit their measured values exactly. Projected higher order modes do not fit the measured wavelength exactly but can clearly be matched with specific peaks which all show a shorter wavelength than expected by the model. Modes $02, 11, 20$ and $03, 12, 21, 30$ and $40, 31, 22, 13, 04$ seem to fit the spectral peaks number $4-6$, $7-10$ and $11-15$. The mismatch of the projections with shorter measured wavelengths leads to discussion for a possible enhancement of the theoretical model in Sect. 3.6.

Since a spectrometer is generally polarization dependent we placed a polarizer in front of the spectrometer and rotate a $\lambda/2$ waveplate in the part towards the spectrometer (and polarizer). The polarization of a single mode maximizes every $\Delta\theta = \pi/2$ angles. For a given $\Delta\theta$ Fig. 3.15 plots two spectra of opposite polarization. For higher order modes, that is at lower wavelength, it is obvious that the modes maximize at different angles. The spectral splitting between the same modes seem to increase with decreasing wavelength. There is a clear spectral splitting even between the two polarization peaks of the fundamental mode, which in the other graph can almost only be identified as a vertical line. The next chapter describes a method how the splitting of the fundamental mode can easily be measured with a higher resolution than the limited CCD array resolution by means of Lorentzian fitting of the peaks. At this point it is important to understand that the fundamental transverse cavity mode exhibits a very good spatial Gaussian shape as shown before and that it divides into two orthogonally-polarized submodes ($M_A^{[00]}$ and $M_B^{[00]}$). This is important for the hole burning technique presented in the next chapter where higher order modes seem to change differently when introducing stress.

A question that comes to mind when looking at the spatial scans is the relative orientation of the modes with respect to the cavity trenches. We analyzed three different samples of which two samples were etched with four trenches and one sample with three trenches. Having analyzed many cavities on the same sample with their trenches having the same orientation relative to the crystal orientation of the substrate, the mode orientation stayed the same.

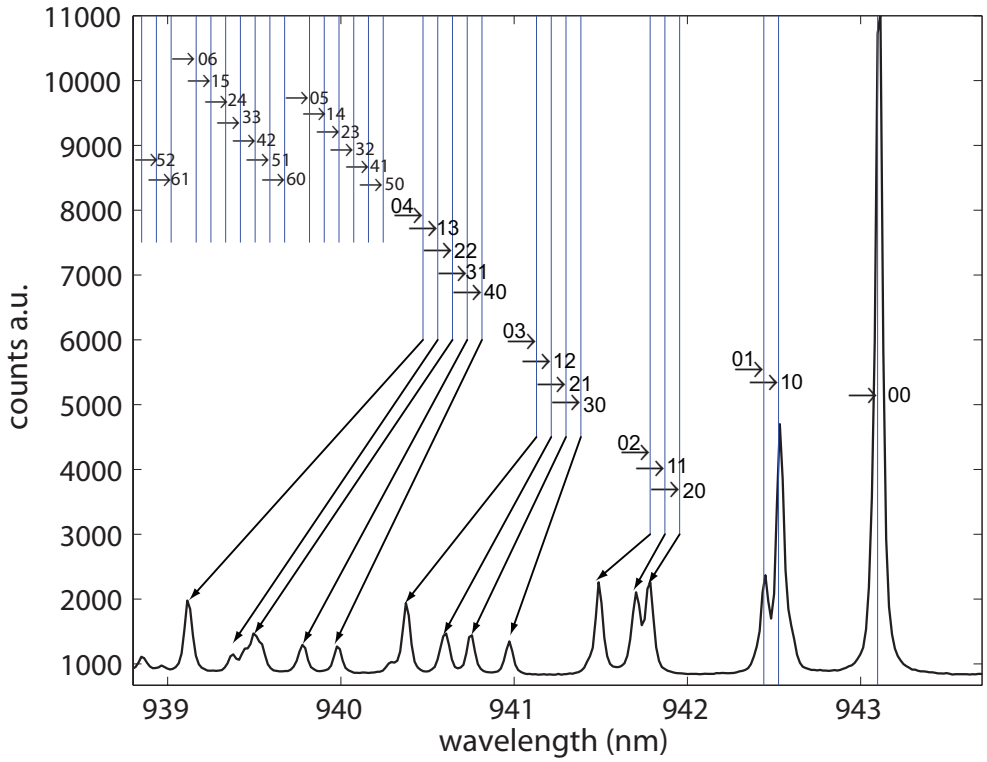

Figure 3.14: *Polarization resolved spectrum with projected modes illustrated as vertical lines. As the result of extracting the model parameters mode* 00, 01 *and* 10 *match the measured wavelength exactly. Higher order modes can be matched with the measured peaks which all show a shorter wavelength than projected by the model.*

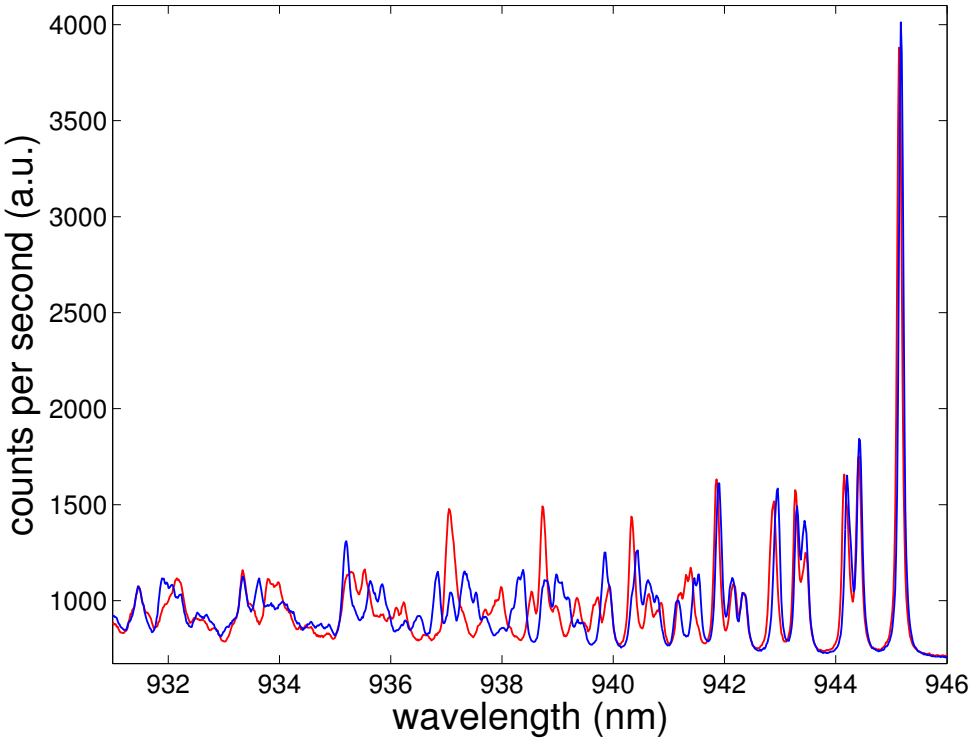

Figure 3.15: *Orthogonal polarization spectra with a polarizer angle difference of* $\Delta\theta = \pi/2$ *maximized on each polarization of the fundamental mode. Towards lower wavelength the spectral splitting of the two polarizations of each mode increases.*

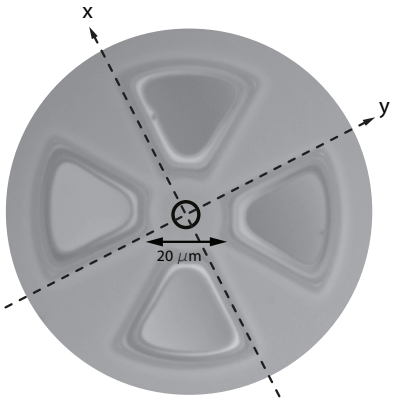

Figure 3.16: *Preferred polarization axes relative to the etched trenches. Top view of a micropillar cavity image showing the four trenches. A circle in the center illustrates the position of the optical cavity. The x and y lines forming a cross illustrate the preferred polarization axes along the etched trenches.*

The measurements indicate that the preferred polarization axes coincide with the edges of the trenches as illustrated in Fig. 3.16 by the lines x and y.

3.6 Improving the theoretical model

In the previous section measurement results show that the theoretical model projecting the modes is lacking accurate predictions for higher order modes. Though the sequence of the projected modes is correct, the higher order modes spectrally need to shift to lower wavelengths (compare Fig. 3.14). We confirm this for all our measurements carried out on three different samples with tens of nominally identical structures. This indicates that the experimental mode frequency distribution appears to be super-linear, suggesting that the refractive index profile might be steeper than quadratic.

We use the quadratic potential model which leads to Hermite-Gaussian beams as a first order approximation to the cavity modes. As a first correction we introduce asymmetry in the transversal plane, modeled as a slightly different quadratic potential in two orthogonal transversal directions which we denote as the x and y directions. Those directions turn out to be determined by etched edges of the trenches, indicating that strain is the dominant effect for inducing asymmetry. With this simple elliptical model we can identify up to 10 transversal modes by comparing theoretical mode patterns to the measured mode profiles.

For a better match of the higher order modes, we have tried several approaches to enhance the model. In a first attempt we applied a perturbation to the refractive index assumption in Eq. (3.5). Given the wave function describing our system

$$\psi_{[nm]}(x,y) = H_n(\frac{\sqrt{2}x}{w_x}) \cdot H_m(\frac{\sqrt{2}y}{w_y}) \cdot e^{-\left(\frac{x^2}{w_x^2}+\frac{y^2}{w_y^2}\right)} \tag{3.47}$$

we added a perturbation term changing the potential

$$\langle\psi_0|V|\psi_0\rangle \rightarrow \int dx \int dy f_{nm}^* \cdot f_{nm} \cdot perturbation. \tag{3.48}$$

None of the following perturbations that we could solve analytically let to a significantly better result:

- Perturbation with linear factor

$$\langle\psi_0|V|\psi_0\rangle \rightarrow \int_0^{+\infty} dx \int_0^{+\infty} dy f_{nm}^* \cdot f_{nm} \cdot |x| \tag{3.49}$$

- Perturbation with quadratic factor

$$\langle\psi_0|V|\psi_0\rangle \rightarrow \int dx \int_0^{+\infty} dy f_{nm}^* \cdot f_{nm} \cdot x^2 \tag{3.50}$$

$$\langle\psi_0|V|\psi_0\rangle \rightarrow \int dx \int_0^{+\infty} dy f_{nm}^* \cdot f_{nm} \cdot y^2 \tag{3.51}$$

$$\langle\psi_0|V|\psi_0\rangle \rightarrow \int dx \int_0^{+\infty} dy f_{nm}^* \cdot f_{nm} \cdot x \cdot y \tag{3.52}$$

- Perturbation with quartic factor

$$\langle\psi_0|V|\psi_0\rangle \rightarrow \int dx \int_0^{+\infty} dy f_{nm}^* \cdot f_{nm} \cdot x^4 \tag{3.53}$$

$$\langle\psi_0|V|\psi_0\rangle \rightarrow \int dx \int_0^{+\infty} dy f_{nm}^* \cdot f_{nm} \cdot y^4 \tag{3.54}$$

$$\langle\psi_0|V|\psi_0\rangle \rightarrow \int dx \int_0^{+\infty} dy f_{nm}^* \cdot f_{nm} \cdot x^2 \cdot y^2 \tag{3.55}$$

Nevertheless, the results indicated that a small correction for the higher order modes of linear or quadratic type could improve the quantitative agreement between the predicted mode frequencies and the measured frequencies.

In a second attempt we introduced a linear stretching of the spectra. In graph 3.17 we plot, for one polarization, the experimental mode wavelength measured (horizontal axis) versus the theoretical wavelength of the projected mode (vertical axis) calculated with the parabolic refractive index profile. We then fit a linear curve through the data points. Identification of peaks up to number 17 is non-ambiguous (supported by spatial scans). The additional 13 data points are mapped by wavelength only (which also maps the first 17 peaks correctly). This graph indicates that the transversal confinement potential of our micropillars has a small correction of a linear potential for higher order modes (which in this measurement roughly scales with $y = 0.6142 \cdot x + 363.6\text{nm}$). This result could be explained looking at the shape of the oxide-aperture (compare Fig. 3.7(b)). The oxide-aperture exhibits a linear sharp edge which stops before reaching the center of the cavity during the oxidation process. Figure 3.18 depicts the projections for the first 15 peaks when applying the linear shift for each mode. For higher order modes the linear shift allows to match the sets of peaks much better than compared to graph 3.14. For the first few modes the error is quite large. The fact that the oxidation front does not reach all the way to the middle could explain the rather large error for the 00-mode (longest wavelength) when applying the linear shift to all modes.

The discussion of a possible model enhancement led to the idea of reconstructing the refractive index potential from the measurements. In order to do so we characterized the spatial mode patterns of another microcavity in detail. Figure 3.19 shows the measured mode wavelength vs. the theoretical mode wavelength calculated with the parabolic refractive index profile in Eq. (3.5). The experimental mode frequency distribution appears to be super-linear, suggesting that the refractive index profile might be steeper than quadratic.

Using the mathematical analogy between the Helmholtz equation and the Schrödinger equation, reconstruction of the refractive index profile is equivalent to reconstructing a potential. Expressing the stationary Schrödinger equation

$$H\psi = E\psi \tag{3.56}$$

in the form

$$\left(-\frac{\hbar^2}{2m}\nabla^2 + V\right)\psi = E\psi, \tag{3.57}$$

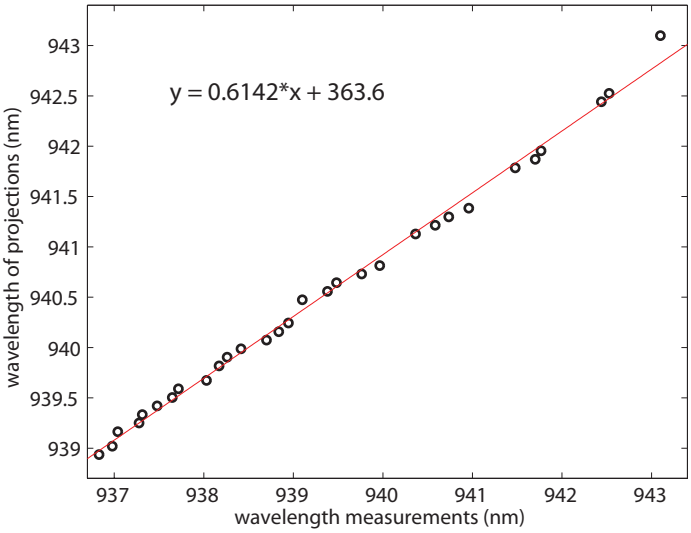

Figure 3.17: *Presented is the wavelength of the projected peaks vs. the measured peaks of the spectral measurements. Fitting a linear curve yields a shift for the projections.*

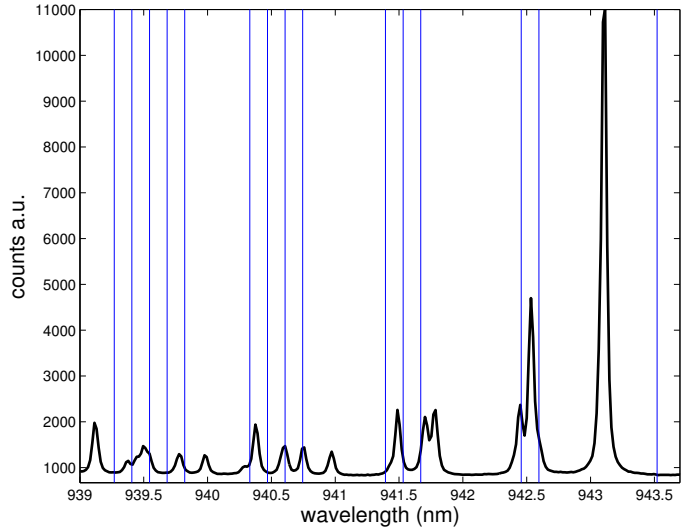

Figure 3.18: *Projections applied to linear fit. Based on the fit from graph 3.17 the new projections are calculated (vertical lines). The error is rather large for the first few lower order modes. But the sets of modes fit the sets of peaks much better than compared to graph 3.14.*

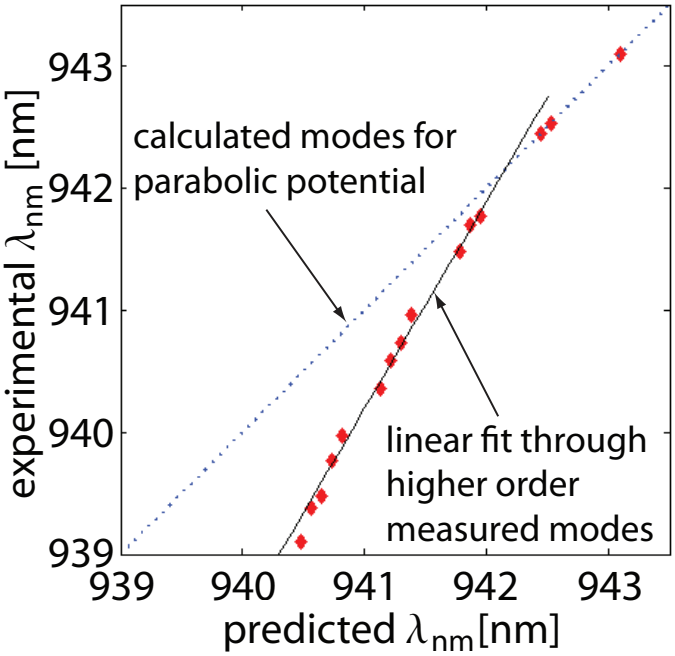

Figure 3.19: *Super-linear mode frequency distribution of the first 15 modes. For higher order modes the experimental mode frequency distribution shows a super-linear behaviour while the theoretical modes described by the parabolic potential match the first three modes.*

for a wave function ψ we can analogously write the Helmholtz equation as

$$\nabla^2\psi + n^2k^2\psi = 0 \tag{3.58}$$

with n being the index profile and k the free-space wavenumber. Solving for the potential, we express the Hamiltonian in terms of its complete set of orthonormal eigenfunctions $H = \sum_{n=1}^{\infty} \varepsilon_n \mid n\rangle\langle n \mid$ and calculate it in the x-representation, we get:

$$V(x) = \langle x \mid H \mid x\rangle = \sum_{n=1}^{\infty} \varepsilon_n |\psi_n(x)|^2 \tag{3.59}$$

Since only a finite number of modes N can be experimentally measured, we normalized over $\sum_{n=1}^{N} |\psi_n(x)|^2$ so that the potential becomes

$$V(x) = \frac{\sum_{n=1}^{N} \varepsilon_n |\psi_n(x)|^2}{\sum_{n=1}^{N} |\psi_n(x)|^2}. \tag{3.60}$$

Before applying the reconstruction to our measurements, we want to see what we can expect theoretically. Therefore we solve the Helmholtz equation $\nabla^2\psi(x) + k_0^2 n^2(x)\psi(x) = 0$ numerically. Discretization leads to the finite-difference expression:

$$\varepsilon\psi_n = k_0^2 n^2(x)\psi_n + t_0[2\psi_n - \psi_{n-1} - \psi_{n+1}], \tag{3.61}$$

$t_0 = 1/a^2$ being the discrete step. Eigenvalues and eigenfunctions are found diagonalizing the matrix:

$$U_{ij} = k_0^2 n^2(x_i)\delta_{ij} + t_0[2\delta_{ij} - \delta_{i,j-1} - \delta_{i-1,j}]. \tag{3.62}$$

In Fig. 3.20 we model the eigenvalue distributions for different potentials. For a parabolic potential (Fig. 3.20(a)) the eigenvalues increase linear with the mode number (Fig. 3.20(b)). If we model the potential V steeper than the parabolic potential (Fig. 3.20(c)) we obtain a super-linear correlation between the eigenvalues and the mode number (Fig. 3.20(d)). On the contrary, for a potential with a less steep slope compared to the parabolic potential (Fig. 3.20(e)) the correlation is sub-linear (Fig. 3.20(f)).

The experimental results, shown in Fig. 3.21 confirm that the refractive index profile is not quadratic, but consists of a flat bottom that corresponds to the un-oxidized region surrounded by steeper walls resulting from the end of the oxidation front. Figure 3.21(b) plots the data-points for the cross-section of the potential along the line indicated in Fig. 3.21(a). The solid line shows the parabolic fit of the bottom of the curve. The results are in agreement with a super-linear description of the potential for higher order modes.

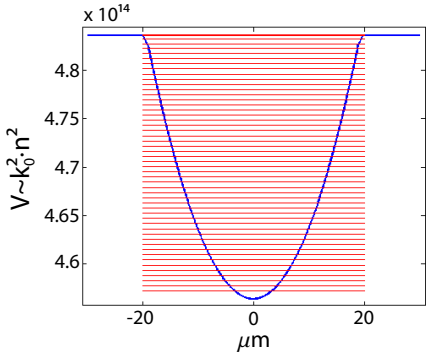

(a) parabolic potential

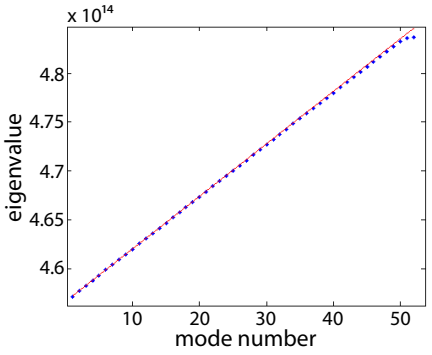

(b) linear correlation

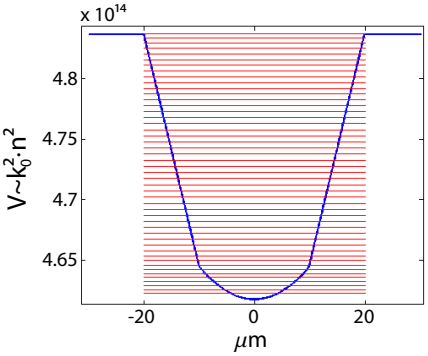

(c) steeper potential

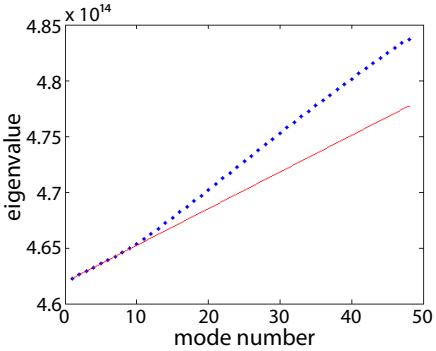

(d) super-linear correlation

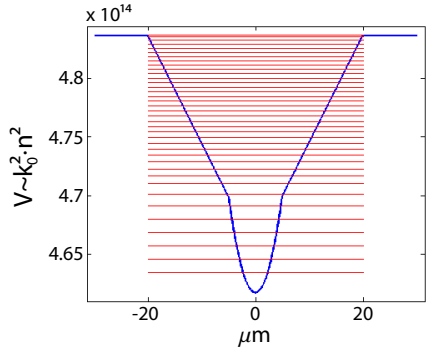

(e) less steep slope

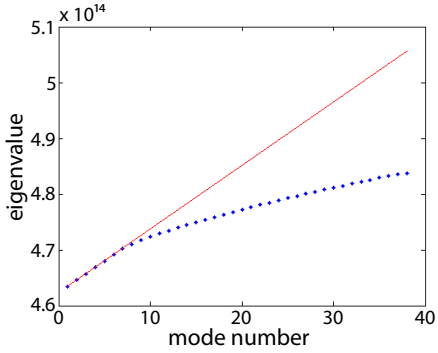

(f) sub-linear correlation

Figure 3.20: *Eigenvalue distributions for different potentials. Left column shows the potential modeled with its correlation between the eigenvalue and mode number plotted on the right.*

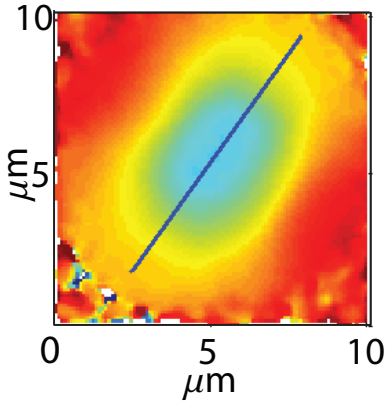

(a) 2D density plot of the reconstructed refractive index profile.

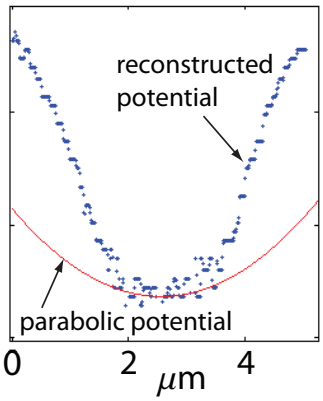

(b) Cross section of reconstruction and partial parabolic fitting

Figure 3.21: *Reconstruction of the refractive index profile.*

3.7 Conclusion and discussion

In conclusion, we have developed a propagation model that explains the frequency of the transverse modes. The propagation model assumes cylindrical quadratic refractive index variation from the center of the cavity at least for the lower order modes. We have demonstrated that the fundamental mode almost perfectly exhibits a Hermite-Gaussian profile, which can be of use for Gaussian beam calculations and for very efficient coupling to external modes. This supports the implementation of the scalable hybrid quantum information schemes described in Chap. 7. Matching an external field to the cavity with a very high accuracy is crucial for the fidelity of the entanglement process involved. Only then micropillar cavities could be the building block for scalable quantum information processing [68]. Higher order modes cannot be precisely matched with the theoretical model and show a super-linear behavior. For a better understanding of these higher order modes and the role of the oxide-aperture we discussed a technique to retrieve the shape of the confining refractive index distribution determined by the oxidation layer, showing that it is shallower in the center with steep walls. This profile explains the super-linear distribution of the confined modes.

We have studied tens of nominally identical structures and we have almost always seen a clear directional difference between the spot sizes w_x and

w_y. Experimentally we observe that the cavity modes have preferred polarization axes which coincide with the edges of the trenches suggesting that strain (by local deformation) is the dominant reason for the observed anisotropy. Therefore we introduced polarization into the discussion. The polarization properties of the micropillar cavities are at least influenced by three issues.

1. The crystal orientation.
2. The properties of the oxidation front, which is determined by the geometry of the etched trenches and the oxidation rate along different crystal axes.
3. Strain in the material.

The samples remained exhibiting Hermite-Gaussian profiles for the fundamental mode when the cavity was polarization degenerate. For higher order modes with active emitters and close to polarization degenerate cavities we have seen indications that support the Laguerre type of modes.

Having a clear understanding of in particular higher order modes can help and improve positioning of such nanostructures relative to emitters [69]. Features from higher order modes can be seen with a larger radius and distance from the cavity center which could be of advantage over scanning only e.g the fundamental mode. The latter mode would also not give any insight into the relative polarization axes in respect to device properties like i.e. trench locations. In the case of a single-mode optical cavity, the emission pattern as seen through one of the cavity mirrors is the profile of that cavity mode. But the radiation pattern becomes nontrivial and strongly dependent on the position of the emitter if the cavity supports several frequency-degenerate modes [70] allowing to track single emitters.

We derived a formula to estimate the theoretical maximum Purcell factor from the splitting between the fundamental and the first-order modes, which can be used to quickly assess the quality of a device for cavity-QED experiments. The measurement techniques developed are very important for further experiments described in the next chapters. Gaussian-fitting of modes measured by polarization resolved spectra allow for a quick analysis of the degree of polarization degeneracy of a cavity during the active process of reducing the splitting of the fundamental mode. Spatial scans provide an opportunity to locate relative positions of emitters and cavity features and are of importance for interpretation of our results presented in Chap. 8.